

Facile preparation of peanut-shaped cobalt-doped zinc manganese oxide as a cathode for zinc-ion battery

Achanai Buasri^a, Chananchida Patitad^a, Chonthicha Bunnom^a, Phonsawan Butdee^a, Prasit Pattananuwat^b, Vorrada Loryuenyong^{a,*}

^a Department of Materials Science and Engineering, Faculty of Engineering and Industrial Technology, Silpakorn University, Nakhon Pathom, Thailand

^b Department of Materials Science, Faculty of Science, Chulalongkorn University, Bangkok, Thailand

ARTICLE INFO

Article history:

Received 18 June 2025

Accepted 30 January 2026

Available online 26 February 2026

Keywords:

Cathode materials

Zinc-ion batteries

Doping

Co-doped ZnMn₂O₄

Sustainable energy storage

Product innovation

Solvothermal method

ABSTRACT

The peanut-shaped cobalt (Co)-doped zinc manganese oxide (ZMO: ZnMn₂O₄) was successfully synthesized via a simple solvothermal and calcination process. The effects of Co-doping concentration on the structural and electrochemical properties of the samples were examined. The novel porous Zn_{1-x}Co_xMn₂O₄ materials with different molar fractions relative to Zn (where x = 0, 0.15, 0.3, and 0.45) were characterized by X-ray diffraction (XRD), Fourier transform infrared (FT-IR) spectroscopy, ultraviolet–visible–near infrared (UV–Vis–NIR) spectroscopy, field emission scanning electron microscopy (FESEM), energy dispersive X-ray spectroscopy (EDS), and nitrogen (N₂) adsorption–desorption isotherms. The results demonstrated that the incorporation of Co into the ZnMn₂O₄ lattice did not produce any distinct secondary phases. The microparticle size and the specific surface area increased, while the energy band gap was reduced. The application of the peanut-shaped Co-doped ZnMn₂O₄ samples as cathode materials for zinc-ion batteries (ZIBs) was also investigated. The ZMO-0.45Co sample exhibited a larger cyclic voltammetry (CV) peak area, higher redox peak value, and lower charge transfer resistance (R_{ct}) compared to the undoped sample (ZMO-0Co). The maximum charge and discharge capacities were 133.0 and 122.5 mAh g⁻¹, respectively. These results suggest that the Co doping in peanut-shaped ZMO enhances charge transfer efficiency and improves the specific capacity of cathode material in ZIBs.

© 2026 The Authors. Published by Elsevier España, S.L.U. on behalf of SECV. This is an open access article under the CC BY-NC-ND license (<http://creativecommons.org/licenses/by-nc-nd/4.0/>).

Abbreviations: ZIB, zinc-ion battery; LIB, lithium-ion battery; ZMO, zinc manganese oxide; VO, vanadium oxide; PVA, polyvinyl alcohol; PVDF, polyvinylidene fluoride; NMP, N-methyl-2-pyrrolidone; TEA, triethanolamine; DI water, deionized water; 1D, one-dimensional; JCPDS, joint committee on powder diffraction standards; XRD, X-ray diffraction; FT-IR, Fourier transform infrared; IR, infrared; UV–Vis–NIR, ultraviolet–visible–near infrared; FESEM, field emission scanning electron microscopy; EDS, energy dispersive X-ray spectroscopy; BET, Brunauer–Emmett–Teller; BJH, Barrett–Joyner–Halenda; EIS, electrochemical impedance spectroscopy; CPE, constant phase element; CV, cyclic voltammetry; GCD, galvanostatic charge–discharge; IUPAC, International Union of Pure and Applied Chemistry IUPAC.

* Corresponding author.

E-mail address: vorrada@gmail.com (V. Loryuenyong).

<https://doi.org/10.1016/j.bsecv.2026.100487>

0366-3175/© 2026 The Authors. Published by Elsevier España, S.L.U. on behalf of SECV. This is an open access article under the CC BY-NC-ND license (<http://creativecommons.org/licenses/by-nc-nd/4.0/>).

Fácil preparación de óxido de zinc manganeso dopado con cobalto en forma de cacahuete como cátodo para batería de zinc-ion

R E S U M E N

Palabras clave:

Materiales de cátodo
Baterías de zinc-ion
Dopaje
ZnMn₂O₄ dopado con Co
Almacenamiento de energía sostenible
Innovación en productos
Método solvotérmico

El óxido de zinc manganeso dopado con cobalto en forma de cacahuete (Co-ZMO: ZnMn₂O₄) fue sintetizado con éxito mediante un proceso sencillo de solvotermia y calcinación. Se examinaron los efectos de la concentración de dopaje con Co en las propiedades estructurales y electroquímicas de las muestras. Los nuevos materiales porosos de Zn_{1-x}Co_xMn₂O₄, con diferentes fracciones molares respecto al Zn (donde x = 0, 0.15, 0.3 y 0.45), fueron caracterizados mediante difracción de rayos X (DRX), espectroscopía infrarroja por transformada de Fourier (FT-IR), espectroscopía ultravioleta-visible-infrarrojo cercano (UV-Vis-NIR), microscopía electrónica de barrido de emisión de campo (FESEM), espectroscopía dispersiva de energía (EDS) e isotermas de adsorción-desorción de nitrógeno (N₂). Los resultados demostraron que la incorporación de Co en la red de ZnMn₂O₄ no produjo fases secundarias distintas. El tamaño de micropartículas y la superficie específica aumentaron, mientras que la banda de energía se redujo. También se investigó la aplicación de las muestras de Co-dopado en forma de cacahuete como materiales de cátodo para baterías de zinc-ion (ZIBs). La muestra ZMO-0.45Co mostró un área de pico mayor en voltametría cíclica (CV), un valor de pico redox más alto y una resistencia de transferencia de carga (R_{ct}) menor en comparación con la muestra sin dopar (ZMO-0Co). Las capacidades máximas de carga y descarga fueron de 133,0 y 122,5 mAh g⁻¹, respectivamente. Estos resultados sugieren que el dopaje con Co en el ZMO en forma de cacahuete mejora la eficiencia de transferencia de carga y aumenta la capacidad específica del material de cátodo en las ZIBs.

© 2026 Los Autores. Publicado por Elsevier España, S.L.U. en nombre de SECV. Este es un artículo Open Access bajo la CC BY-NC-ND licencia (<http://creativecommons.org/licencias/by-nc-nd/4.0/>).

Introduction

The increasing consumption of fossil fuels and escalating environmental issues have led to a significant demand for efficient and sustainable energy storage systems. These systems must be capable of extracting energy from renewable and clean sources such as solar, wind, geothermal, and wave power. Among various energy conversion and storage technologies, electrochemical devices are particularly favored due to their compact design and suitability in portable electronics [1–3]. This growing demand has greatly contributed to the widespread development of solar cells, fuel cells, sensors, smart windows, supercapacitors, electrification, and rechargeable batteries [4–9].

Batteries are among the most efficient energy storage devices for retaining electricity when renewable sources are unavailable. They can be categorized into two types: (i) primary batteries, which are used once and discarded, and (ii) secondary batteries, which can be recharged and reused multiple times [10–12]. Lithium-ion batteries (LIBs) are currently the dominant commercial energy storage technology due to their high energy density and long cycle life. However, their widespread application is constrained by safety concerns, high production costs, limited lithium resources, and the use of flammable organic electrolytes. In contrast, zinc-ion batteries (ZIBs) have emerged as a promising alternative to LIBs for large-scale and safe energy storage systems. They offer several advantages, including low assembly cost, abundant zinc (Zn) resources, environmental sustainability, high

theoretical capacity, low redox potential, and the nonflammability and high ionic conductivity of aqueous electrolytes [13]. A typical ZIB device generally consists of four main components: (i) an anode, (ii) a cathode, (iii) a separator, and (iv) an electrolyte [14–17]. Despite the advantages of ZIBs, selecting appropriate cathode materials remains a significant challenge. Manganese dioxide (MnO₂), zinc manganese oxide (ZMO: ZnMn₂O₄), and vanadium oxide (VO: V₂O₅) have been widely investigated as cathode materials for ZIBs due to their numerous crystal phases and high working potential. Among these, ZMO is considered as a particularly attractive candidate for both cathode and anode materials in ZIBs [18–21]. It is a typical binary transition metal oxide with a spinel structure that can be synthesized in various morphologies, including loaf-like structure, flower-like superstructure, hollow microsphere, and one-dimensional (1D) nanostructures. ZMO consists of bivalent Zn²⁺ ions located at tetrahedral sites and trivalent manganese (Mn³⁺) ions situated at octahedral sites [22,23]. However, pristine ZMO exhibits particle aggregation, low intrinsic electronic conductivity and significant volume variation during the charge-discharge cycles. These issues cause manganese (Mn) dissolution, electrode polarization, loss of inter-particle electrical contact, ultimately resulting in poor rate capability and cycling stability. To address these problems, structural engineering strategies such as morphological design, porosity control, and compositional modification have been investigated to improve the electrochemical performance of ZMO-based electrodes [24–26].

Recently, several researchers have investigated semiconductor materials doped with small amounts of dopants to

improve their physical and electrochemical properties [27,28]. In order to achieve the desirable structural properties, the transition metal ions were doped into ZnMn_2O_4 to incorporate additional positive carriers inside the host material. The preparation processes, along with the type and concentration of doped elements, can be modified to enhance the properties of ZnMn_2O_4 by modifying its crystal structure and energy band configuration [29,30]. The improvement of specific capacitance is mostly due to the synergistic effect of multi-metal ions and the increased porosity of the structures. The incorporation of metal ions into ZnMn_2O_4 can significantly reduce charge resistance and enhance charge transport rates, thereby accelerating reaction kinetics [31,32]. Among various dopants, cobalt (Co) has shown great potential due to its favorable ionic radius and multiple oxidation states. The ionic radius of Co^{2+} (0.745 Å) is comparable to that of Mn^{3+} (0.785 Å), allowing Co ions to substitute Mn sites in the ZnMn_2O_4 spinel lattice without causing significant lattice distortion. This substitution can enhance electrical conductivity, stabilize Mn oxidation states, and suppress Mn dissolution by strengthening the metal–oxygen (M–O) framework. Additionally, the synergistic redox activity between Co and Mn ions improves charge transfer kinetics and facilitates reversible Zn^{2+} intercalation and deintercalation, leading to superior capacity retention, rate performance, and structural stability of ZMO-based electrodes.

Sk.K. Hussain and J.S. Yu [31] focused on the development of Co-doped Zn–Mn oxide nanocubes with porous morphology for enhanced performance as positive electrodes in hybrid supercapacitors. The Co doping in ZnMn_2O_4 has been shown to enhance electrochemical performance through improving electrical conductivity and an increase in active sites for redox reactions. The resulting porous nanocube morphology provided a large surface area and enhanced ion diffusion, thereby improving overall performance. X. Zhu et al. [30] investigated the effects of Co doping on the properties of ZnMn_2O_4 . The obtained samples exhibited loose hollow microsphere structures. It was found that Co doping significantly enhances photocatalytic activity and electrochemical properties, rendering the resultant materials suitable for pollutant degradation and as electrode materials for hybrid supercapacitors. However, to the best of our knowledge, publications examining the effects of Co doping on the microstructure and electrochemical characteristics of ZnMn_2O_4 in ZIBs remain limited and require further exploration.

Herein, we report a simple and cost-effective solvothermal method for the preparation of peanut-shaped Co-doped ZnMn_2O_4 . All samples were thoroughly characterized using various complementary techniques, including X-ray diffraction (XRD), Fourier transform infrared (FT-IR), ultraviolet–visible–near infrared (UV–Vis–NIR) spectroscopy, field emission scanning electron microscopy (FESEM), energy dispersive X-ray spectroscopy (EDS), and nitrogen (N_2) adsorption–desorption isotherms. Furthermore, the synthesized Co-doped ZnMn_2O_4 porous materials were subsequently employed as electrode materials for ZIBs. A ZIB device was constructed by assembling the optimized Co-doped ZnMn_2O_4 electrode materials as the cathode, Zn electrode materials as the anode, and polyvinyl alcohol (PVA) as the polymer separator to evaluate its practical performance. The effects of

Co doping on the electrochemical and electrical properties of ZnMn_2O_4 -based ZIBs were systematically investigated.

Experimental

Chemical reagents

Zinc acetate dihydrate ($\text{Zn}(\text{CH}_3\text{COO})_2 \cdot 2\text{H}_2\text{O}$), 99.5%, AR, LOBA CHEMIE PVT. LTD., Mumbai, India; Manganese (II) acetate tetrahydrate ($\text{Mn}(\text{CH}_3\text{COO})_2 \cdot 4\text{H}_2\text{O}$), 98.5%, AR, LOBA CHEMIE PVT. LTD., Mumbai, India; Cobalt (II) acetate tetrahydrate ($\text{Co}(\text{CH}_3\text{COO})_2 \cdot 4\text{H}_2\text{O}$), 98.0%, AR, Himedia™, Maharashtra, India; Urea ($\text{CH}_4\text{N}_2\text{O}$), 99.0%, AR, KemAus™, New South Wales, Australia; Triethanolamine (TEA: $\text{N}(\text{CH}_2\text{CH}_2\text{OH})_3$), 99.0%, AR, KemAus™, New South Wales, Australia; All of the chemical reagents mentioned above were employed directly during the experiment without any additional purification. The deionized (DI) water used in the experiment was self-produced.

Synthesis of porous materials

Initially, 1 mmol of $\text{Zn}(\text{CH}_3\text{COO})_2 \cdot 2\text{H}_2\text{O}$, 2 mmol of $\text{Mn}(\text{CH}_3\text{COO})_2 \cdot 4\text{H}_2\text{O}$, and 0.06 mol of $\text{CH}_4\text{N}_2\text{O}$ were solubilized in 30 mL of DI water and TEA (1:1 v/v) under continuous stirring for 30 min. Subsequently, the obtained homogenous solution was transferred to a 50 mL Teflon-lined stainless-steel autoclave and heated at 160 °C for 12 h, leading to the production of white precursors. The Zn–Mn precursors were then separated using centrifugation and rinsed several times with DI water and ethanol ($\text{C}_2\text{H}_5\text{OH}$). After drying, the Zn–Mn precursors were calcined in air at 800 °C for 5 h to provide the final ZnMn_2O_4 porous materials [26,33–35]. Fig. 1 illustrates the straightforward synthesis of peanut-shaped ZnMn_2O_4 particles via the solvothermal method utilizing the beginning components. The same procedure was employed to synthesize Co-doped ZnMn_2O_4 products. Specifically, $\text{Zn}_{1-x}\text{Co}_x\text{Mn}_2\text{O}_4$ samples with varying dopant concentrations of $\text{Co}(\text{CH}_3\text{COO})_2 \cdot 4\text{H}_2\text{O}$ relative to Zn ($x=0, 0.15, 0.3, \text{ and } 0.45$) were prepared. The resultant materials, designated as ZMO-0Co, ZMO-0.15Co, ZMO-0.3Co, and ZMO-0.45Co, were obtained and used for further investigations.

Characterization of porous materials

The crystallographic data for calcined and synthesized samples was analyzed using a LabX XRD-6100 device (Shimadzu, Kyoto, Japan) with $\text{Cu K}\alpha$ radiation at $\lambda=0.15418$ nm. The target voltage was 30 kV, while the current was 20 mA. The scanned 2θ range was 10–80°, with a step size of 0.04° and a rate of 4°/min. FT-IR spectra were recorded using a VERTEX 70 v instrument (BRUKER, Leipzig, Germany) with a potassium bromide (KBr) pellet in the wavelength range of 2000–450 cm^{-1} . A UV–Vis–NIR spectrophotometer (UV-3600i Plus, Shimadzu, Kyoto, Japan) was employed to assess the light absorbance of powder samples, recording in absorbance and reflection mode across a wavelength range of 200–800 nm, with barium sulfate (BaSO_4) as a reference standard. The morphologies and microstructures of the products were

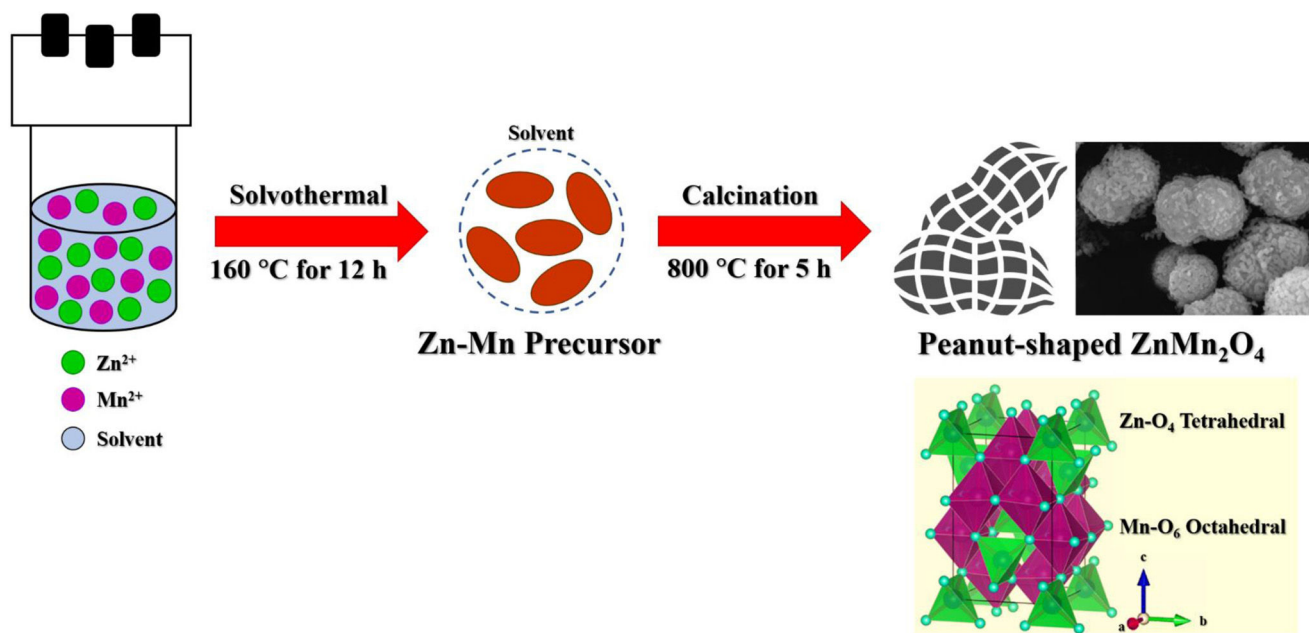


Fig. 1 – Schematic diagram of the synthesis procedure of peanut-shaped ZnMn_2O_4 .

analyzed using FESEM (MIRA3, TESCAN, Brno-Kohoutovice, Czech Republic). The elemental and compositional analysis of the produced samples was investigated using EDS. The N_2 adsorption-desorption isotherms were conducted using an Autosorb IQ-MP (3 STAT) apparatus (Anton Paar Germany GmbH, Ostfildern-Scharnhausen, Germany) with liquid N_2 at 77 K. The Brunauer-Emmett-Teller (BET) method was employed to determine the specific surface areas of peanut-shaped cobalt-doped ZnMn_2O_4 . The pore size distributions were determined utilizing the Barrett-Joyner-Halenda (BJH) method [22,25,36].

Assembly of coin cells for Zn//ZMO and Zn//Co-doped ZMO batteries

ZIBs were fabricated using Zn foil as the anode material in a standard coin cell configuration. For the preparation of cathode materials, $\text{Zn}_{1-x}\text{Co}_x\text{Mn}_2\text{O}_4$ (where $x = 0, 0.15, 0.3, \text{ and } 0.45$), carbon black, and polyvinylidene fluoride (PVDF) were mixed in a weight ratio of 70:20:10 and subsequently dispersed in N-methyl-2-pyrrolidone (NMP) as the solvent [37]. The resulting slurry was uniformly coated onto carbon fiber paper with a doctor blade and then dried at 80°C for 12 h in a vacuum oven. Carbon fiber paper was selected as the current collector due to its high electronic conductivity, chemical stability in the aqueous electrolyte, and three-dimensional porous structure, which enhances electrode-current collector contact and facilitates electrolyte penetration. The electrodes were then cut into disks approximately 9.5 mm in diameter. Coin cells of Zn//ZMO and Zn//Co-doped ZMO were assembled applying a PVA separator and 2 M zinc sulfate (ZnSO_4) as the supporting electrolyte. Fig. 2 depicts a schematic illustration of the batteries used in this study. It presents comprehensive details regarding the individual materials employed as the separator, cathode and anode in the ZIBs.

Electrochemical measurement of Zn//ZMO and Zn//Co-doped ZMO batteries

The Nyquist plot of electrochemical impedance spectroscopy (EIS) was recorded for coin cells of Zn//ZMO and Zn//Co-doped ZMO. The measurements were conducted with a chemical impedance analyzer IM3590 (Hioki, Nagano, Japan) at a voltage of 10 mV and a frequency range of 0.1 Hz to 100 kHz. Cyclic voltammetry (CV) of ZIBs was measured using a Potentiostat/Galvanostat (Autolab PGSTAT204, Metrohm AG, Herisau, Switzerland) at a scan rate of 0.5 mV/s within a voltage range of 0.2–2.2 V for the initial five cycles. Galvanostatic charge-discharge (GCD) cycle tests were carried out using a battery tester (NEWARE TECHNOLOGY LIMITED, BTS-7.1 software, Hong Kong). The capacity performance of ZIBs utilizing ZMO-0Co and ZMO-0.45Co was evaluated across operating potential voltages of 0.8 to 1.8 V at current densities of 0.05, 0.1, 0.3, 0.5, 0.7, and 1.0 A g^{-1} , with five cycles performed at each current density. Furthermore, constructed ZIBs were tested for prolonged cycling stability for 50 cycles of charging and discharging at series current densities of 0.05, 0.1, 0.3, 0.5, 0.7, and 1.0 A g^{-1} , with 5 cycles per current.

Results and discussion

Materials characterization

Fig. 3(a) presents the XRD pattern of sample without Co-doping. The diffraction peaks of high intensity suggest that ZnMn_2O_4 has a high degree of crystallinity. The observed peak positions were at $18.10^\circ, 29.26^\circ, 31.26^\circ, 32.64^\circ, 36.32^\circ, 38.38^\circ, 44.56^\circ, 51.16^\circ, 54.22^\circ, 58.80^\circ, 60.26^\circ, \text{ and } 64.96^\circ$, corresponding to the crystalline planes of (101), (112), (200), (103), (211), (004), (220), (105), (312), (321), (224), and (400) of ZnMn_2O_4 ,

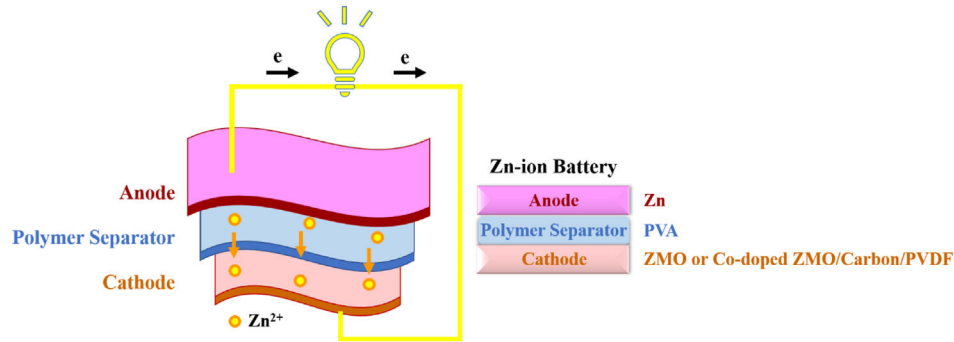


Fig. 2 – A schematic representation of ZIBs.

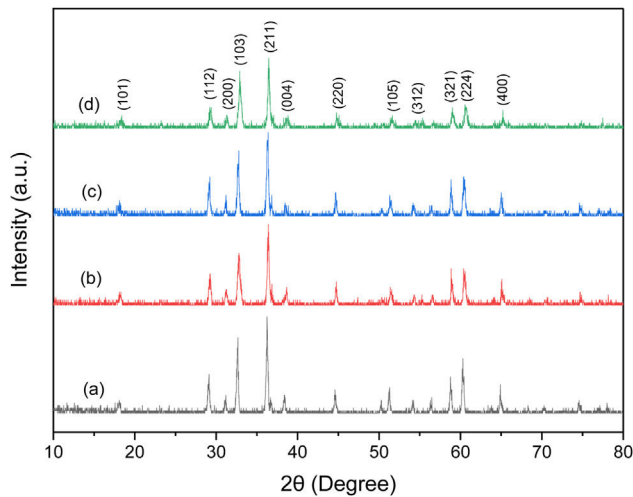


Fig. 3 – XRD patterns of ZnMn_2O_4 at different Co concentrations: (a) ZMO-0Co, (b) ZMO-0.15Co, (c) ZMO-0.3Co, and (d) ZMO-0.45Co.

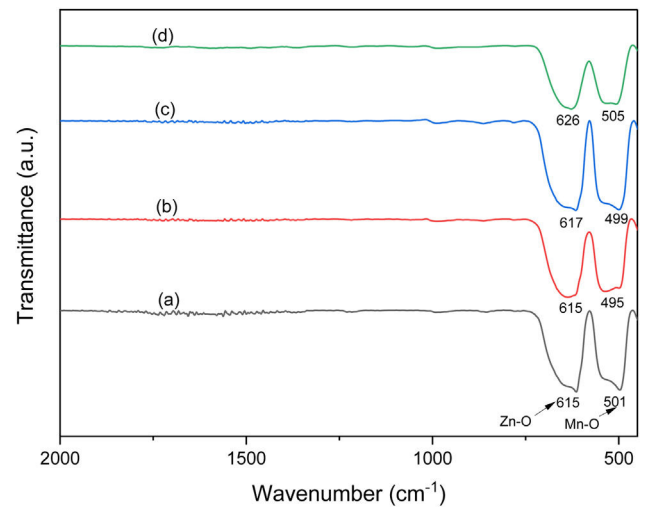


Fig. 4 – FT-IR spectra of ZnMn_2O_4 at different Co concentrations: (a) ZMO-0Co, (b) ZMO-0.15Co, (c) ZMO-0.3Co, and (d) ZMO-0.45Co.

respectively. The indexed diffraction planes indicate that ZnMn_2O_4 exhibits a body-centered tetragonal structure with the $I4_1/amd$ space group [38–42], identified using Joint Committee on Powder Diffraction Standards (JCPDS) Card No. 01-071-2499. The Zn^{2+} bivalent ions normally exhibit significant stabilization at the tetrahedral site, attributed to their $3d^{10}$ electronic configuration, while the Mn^{3+} trivalent ions are found at the octahedral site [43]. Fig. 3(b)–(d) depicts the XRD patterns of Co-doped ZMO nanoparticles at varying Co doping concentrations. All samples exhibited a single-phase structure without detectable impurity peaks. A slight shift of the diffraction peak toward higher angles is observed upon Co-doping, suggesting a modification in lattice parameters [44]. Considering the comparable ionic radii of Co^{2+} (0.72 Å) and Zn^{2+} (0.74 Å), this peak shift is attributed to the substitution of Zn^{2+} by Co^{2+} ions at the tetrahedral sites rather than substitution at Mn^{3+} octahedral sites. Similar substitution behavior has been reported for Co-doped ZnMn_2O_4 spinel systems in previous studies. Therefore, Co^{2+} incorporation is concluded to occur without altering the overall spinel crystal structure, while inducing subtle lattice distortions that may influence electrochemical performance [45,46].

The FT-IR spectra at room temperature were recorded over the range of $2000\text{--}450\text{ cm}^{-1}$, are illustrated in Fig. 4. The data distinctly reveals two absorption bands at approximately 615 cm^{-1} and 501 cm^{-1} , which are associated with the metal-oxygen (O) stretching vibrations in the tetrahedral sites (Zn–O) and metal–O stretching vibrations in the octahedral sites (Mn–O), respectively. The presence of these two bands confirms the formation of spinel ZnMn_2O_4 [47,48]. With increasing Co content, the positions of the absorption band for tetrahedral sites shift toward higher wavenumber, whereas those for the octahedral sites shows minimal alteration, as illustrated in Fig. 4(b)–(d). This may be attributed to the small mass difference between Co^{2+} and Mn^{4+} , along with the limited substitution of Co^{2+} for Mn^{4+} in these sites [49]. The FT-IR spectrum is generally influenced by various factors, including the unit cell parameters, the mass of the cation, the length and strength of the metal–O bond, as well as the doping and distribution of the cation, all of which impact these parameters [50].

The optical characteristics of synthesized ZMO nanoparticles and Co-doped samples were investigated using UV–Vis–NIR measurements. Fig. 5 demonstrates the UV–Vis–NIR absorption spectra for ZnMn_2O_4 and

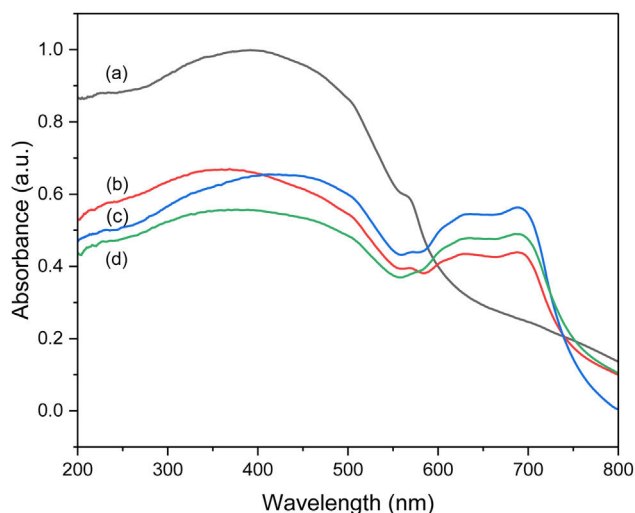


Fig. 5 – Absorption spectra of ZnMn_2O_4 at different Co concentrations: (a) ZMO-0Co, (b) ZMO-0.15Co, (c) ZMO-0.3Co, and (d) ZMO-0.45Co.

$\text{Zn}_{1-x}\text{Co}_x\text{Mn}_2\text{O}_4$ ($x=0.15, 0.3, \text{ and } 0.45$). All samples exhibit a strong optical absorption band in the wavelength range of 300–550 nm, which is an absorption characteristic of ZMO compound. The variation in absorbance between doped and undoped samples may result from the distinct defects, the distribution of various ions, and the interaction between ZMO and Co in the porous materials [50,51]. This phenomenon may be related to the charge transfer that takes place between lattice O and cations [36]. The doped samples also display an additional absorption band in the 600–700 nm region. This band is related to the tetrahedral-coordinated Co^{2+} ions, suggesting that some of the Co^{2+} ions may replace tetrahedrally-coordinated Zn ions [52,53]. The presence of Co^{2+} ions in this coordination is attributed to its ionic radius being comparable to that of Zn ions [54]. This suggests that Co^{2+} ions are capable of effectively substituting for Zn^{2+} ions [55]. In addition, Co doping in ZnMn_2O_4 demonstrates a red shift in energy band gap. The energy band gap of $\text{Zn}_{1-x}\text{Co}_x\text{Mn}_2\text{O}_4$ ($x=0, 0.15, 0.3, 0.45$) are determined to be 1.93, 1.64, 1.63, and 1.59 eV, respectively.

FESEM analysis is performed to investigate the microstructures and grain size of particles, as shown in Fig. 6. The images reveal the oblong microparticles with rounded ends and the constricted central region, commonly described as a peanut-like shape [22,56]. As shown in Fig. 6(a), the undoped sample (ZMO-0Co) exhibited a relatively uniform distribution of rough and porous particles, with an average particle size at approximately $2.42 \mu\text{m}$. The monodisperse microparticles consist of numerous nanoparticles interconnected together to form an irregular, porous microstructure. The specific porous structure of these microparticles is the result of the facile synthesis using the solvothermal method in a Teflon-lined stainless-steel autoclave [57]. Fig. 6(b)–(d) shows the FESEM micrographs of Co-doped ZMO at varying Co concentrations (ZMO-0.15Co, ZMO-0.3Co, and ZMO-0.45Co). All of the samples consist of peanut-shaped grains that precisely correspond to previously reported findings [25,26,58]. The observed

structure has a loose and irregular microsphere morphology, consisting of substantial nanoparticles. As the Co doping content increases, the edges of the microsphere exhibit a looser and hollower structure, leading to the formation of some stacked microspheres that display breakage and hollow characteristics. The hollow microspheres show an increase in size, accompanied by a rougher and more irregular morphology. The presence of this loose hollow microsphere structure enhances the electrochemical performance [29]. Furthermore, the substitution of Zn^{2+} ions with Co^{2+} ions resulted in the creation of oxygen vacancies, which were necessary to maintain the lattice constant and ensure charge impartiality. This substitution induces the formation of a novel lattice configuration, producing a $\text{Zn}_{1-x}\text{Co}_x\text{Mn}_2\text{O}_4$ compound with appropriate electrical and chemical characteristics [59,60]. The transformation of metal ions and the incorporation of oxygen vacancies significantly impacted the modification of the material's chemical and physical properties, as well as its electronic structure, facilitating grain evaluation [61].

EDS was conducted in conjunction with FESEM to evaluate the elemental composition of the materials [35]. To confirm the Co doping within the structure, the ZMO-0.45Co sample was investigated using EDS elemental mapping images. Fig. 7 (top) presents the EDS spectrum of the ZMO-0.45Co sample, showing Zn, Mn, O, and Co chemical components present in the synthesized samples. Fig. 7 (bottom) distinctly demonstrates the distribution of Co within the ZMO microsphere architecture. The Co element exhibits excellent dispersion within the porous structure, with no additional impurities detected. The EDS results support the findings from XRD, FT-IR and UV-Vis-NIR, demonstrating that peanut-shaped Co-doped ZMO was synthesized using a solvothermal method, with Co^{2+} effectively incorporated as a dopant within the ZnMn_2O_4 matrix. Therefore, it is evident that the Co-doping concentration has impacts on the characteristics of peanut-shaped $\text{Zn}_{1-x}\text{Co}_x\text{Mn}_2\text{O}_4$ porous materials [30].

The analysis of the specific surface area and pore characteristics was carried out through N_2 adsorption-desorption studies. The high specific surface area and porosity play an important role in battery and supercapacitor applications, as they enhance the interaction between the electrolyte ion species and the electrode material, leading to improved electrochemical performance [62]. Fig. 8 shows the N_2 adsorption-desorption isotherms for both undoped and Co-doped ZMO nanostructures. The influence of dopant ions is clearly established, impacting both the BET-specific surface area and the distribution of pore sizes [63]. The N_2 adsorption-desorption isotherms of both undoped and Co-doped ZnMn_2O_4 exhibit the characteristic features of a type-IV behavior according to the International Union of Pure and Applied Chemistry (IUPAC) classification data. This suggests that the primary component of all ZnMn_2O_4 materials is mesopores [38,64,65]. Table 1 provides a summary of the specific surface area, pore volume, and average pore size of undoped and Co-doped ZMO. According to the findings, the ZMO-0Co has a BET surface area of $1.29 \text{ m}^2/\text{g}$, a pore volume of $0.0032 \text{ cm}^3/\text{g}$, and an average pore size of 31.16 nm . The ZMO-0.45Co sample demonstrates the optimal surface properties. The surface area, pore volume, and pore size of ZMO-0.45Co

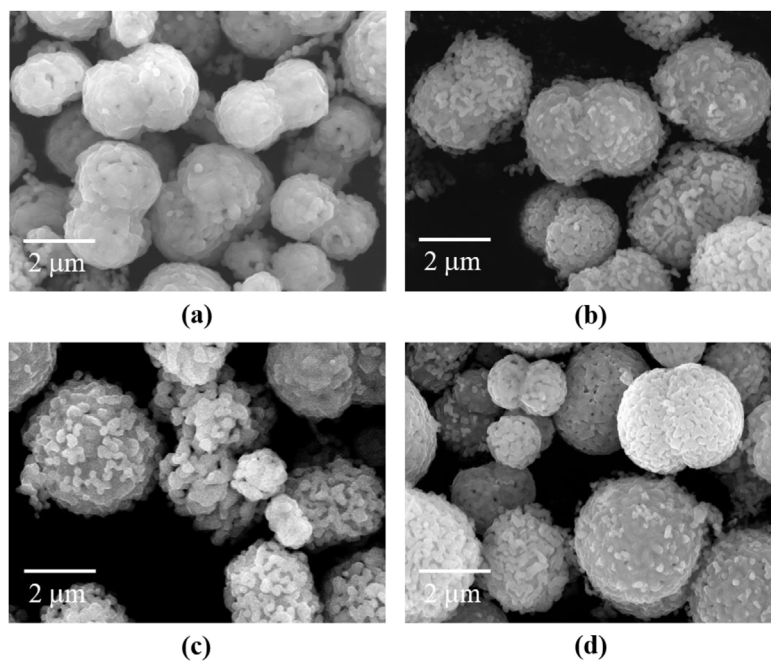


Fig. 6 – FESEM images of ZnMn_2O_4 at different Co concentrations: (a) ZMO-0Co, (b) ZMO-0.15Co, (c) ZMO-0.3Co, and (d) ZMO-0.45Co.

Table 1 – Specific surface area and porosity parameters of ZnMn_2O_4 at different Co concentrations: ZMO-0Co, ZMO-0.15Co, ZMO-0.3Co, ZMO-0.45Co.

Sample	Specific surface area (m^2/g)	Pore volume (cm^3/g)	Average pore size (nm)
ZMO-0Co	1.29	0.0032	31.16
ZMO-0.15Co	2.02	0.0063	34.93
ZMO-0.3Co	1.20	0.0035	20.27
ZMO-0.45Co	2.40	0.0131	57.66

have all increased to $2.40 \text{ m}^2/\text{g}$, $0.0131 \text{ cm}^3/\text{g}$, and 57.66 nm , respectively.

Although the specific surface area does not change considerably, it is shown that both the pore volume and pore size increase significantly. In general, larger pore volume is essential for ion transport, while average pore size could impact capacity. ZMO-0.45Co exhibits a pore size range of up to 200 nm and a pore volume about four times larger than that of undoped samples. The electrochemical performance of the material can be improved by the rapid diffusion of ions between the electrode and the electrolyte. Therefore, this material will be chosen for further investigation of its electrochemical properties. The surface properties that were obtained are comparable to those of several materials that have been previously reported [66,67].

Electrochemical analysis

To investigate the ion storage and diffusion characteristics of the synthesized materials, Zn-ion coin cell batteries were fabricated and subjected to electrochemical testing, as illustrated in Fig. 2. In this research, EIS measurements were employed to evaluate the electrochemical performance of the electrode materials, with particular focus on their resistance characteristics and interfacial electron transfer efficiency [34].

The signal is regulated by kinetic processes at high frequencies, and the charge direction of electron mediator molecules changes prior to the redox reaction occurring at the electrode surface. This fact is a limiting factor (solution resistance: R_s) because it delays the charge transfer across the electrode [68]. The charge transfer resistance (R_{ct}) at the electrode-electrolyte interfaces is correlated with the hemisphere placed in the high frequency region [69]. The EIS curves of the ZMO-0Co and ZMO-0.45Co electrodes are presented in Fig. 9. The impedance spectra were interpreted using an equivalent circuit model consisting of the R_s in series with a parallel combination of R_{ct} and a magnitude (Q) of the constant phase element (CPE), followed by a Warburg diffusion element (Z_w). The curves reveal that Co-doped ZnMn_2O_4 exhibit smaller semicircle radii compared to undoped ZnMn_2O_4 , suggesting the smaller R_{ct} at the interfaces. The Nyquist plots are well fitted with the equivalent circuit of $R_s + (R_{ct} \parallel Q) + Z_w$, as shown in inset Fig. 9. The fitting parameters, with Chi-square values below 5%, are summarized in Table 2. The R_{ct} value of ZMO-0.45Co (48Ω) is lower than that of ZMO-0Co (72Ω). Notably, ZMO-0.45Co exhibits a reduced R_{ct} , accompanied by a higher Q value, indicating faster interfacial kinetics and improved ion diffusion behavior. The presence of Co^{2+} ions may introduce additional active sites and improve the electronic structure, thereby facilitating faster electron transport at the electrode/electrolyte

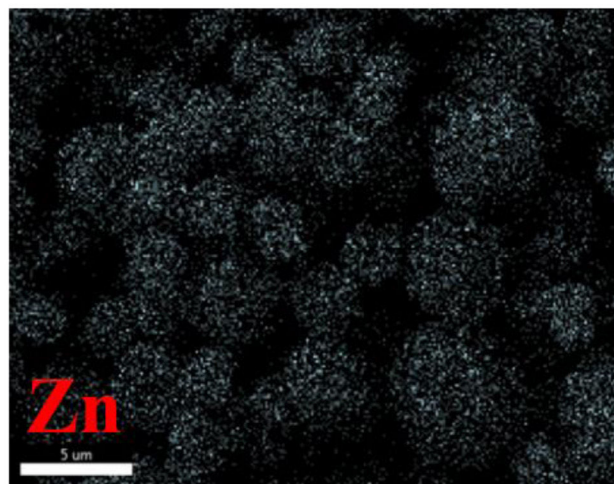
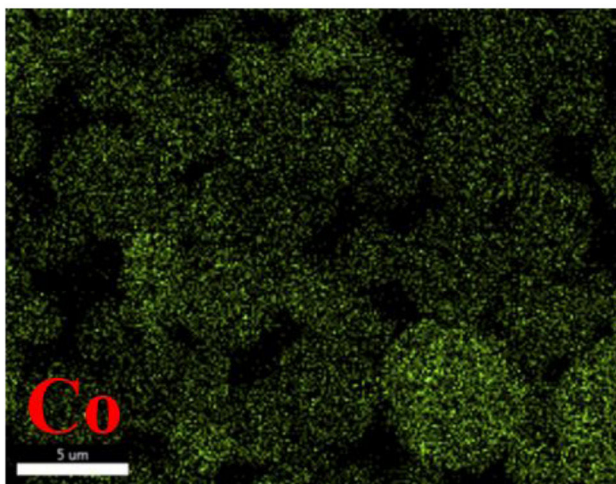
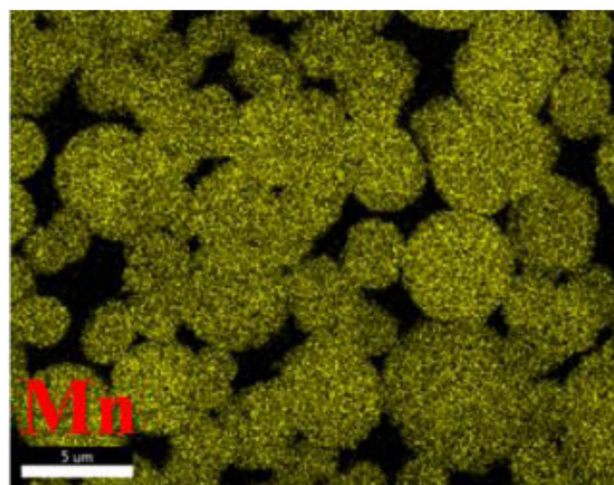
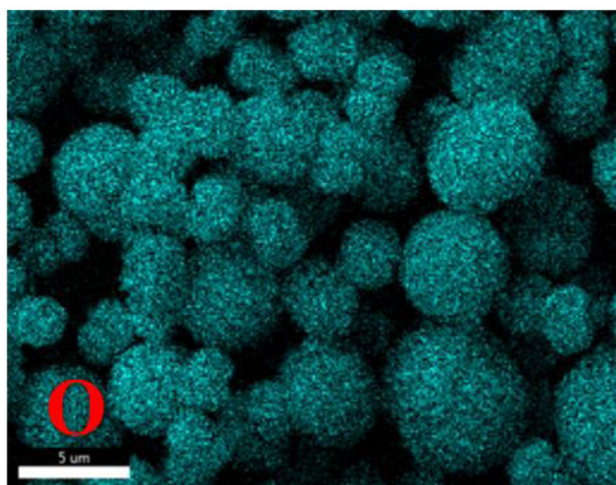
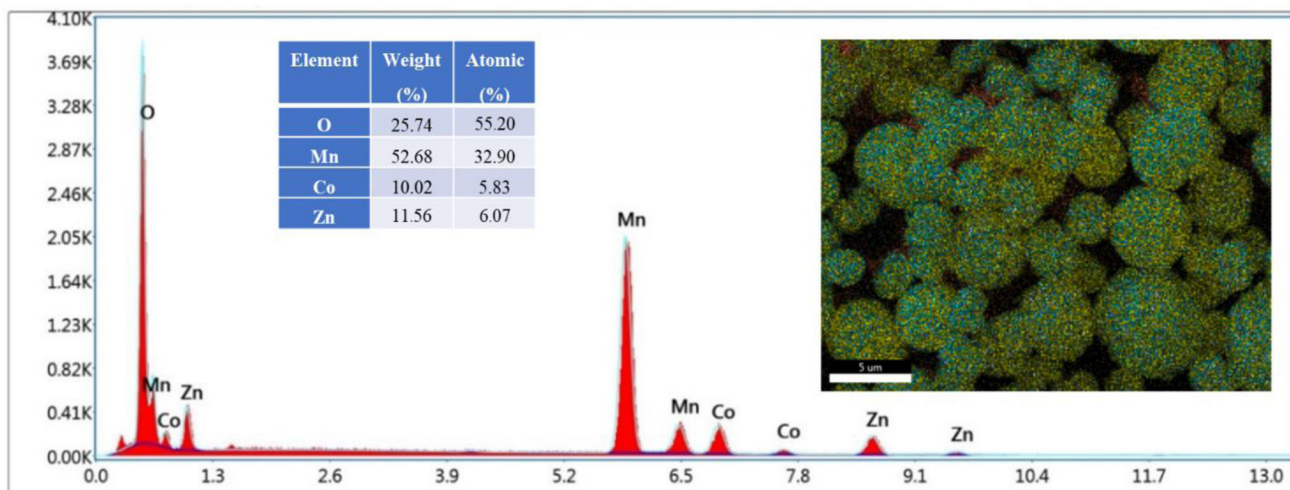


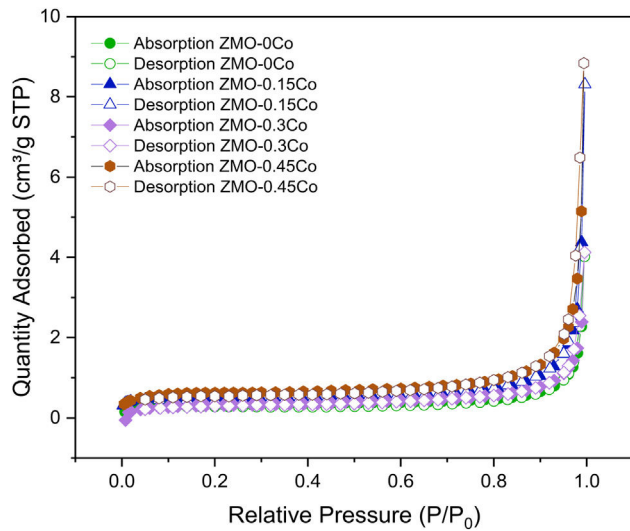
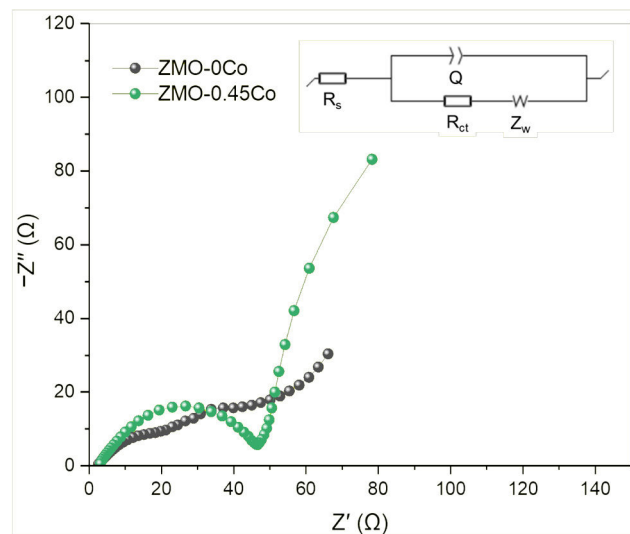
Fig. 7 – EDS spectrum (top), and EDS elemental mapping images of O, Mn, Co and Zn (bottom) of ZMO-0.45Co.

interface. These results quantitatively confirm that Co doping effectively enhances interfacial charge-transfer kinetics. Therefore, the electron transport could be improved by utilizing materials with the porous characteristics [70], such as peanut-shaped cobalt-doped ZMO.

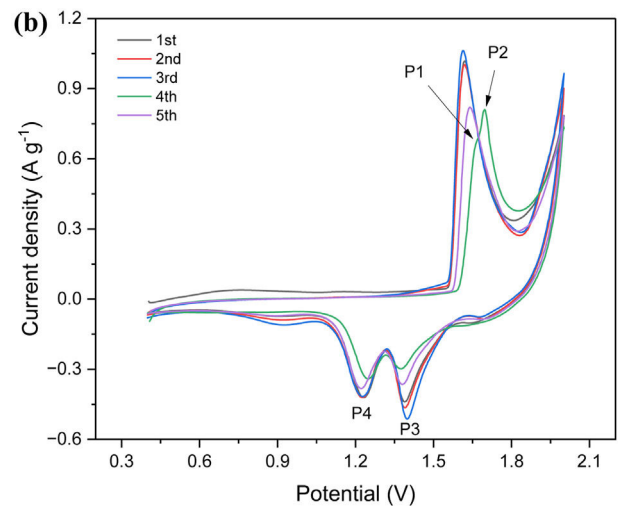
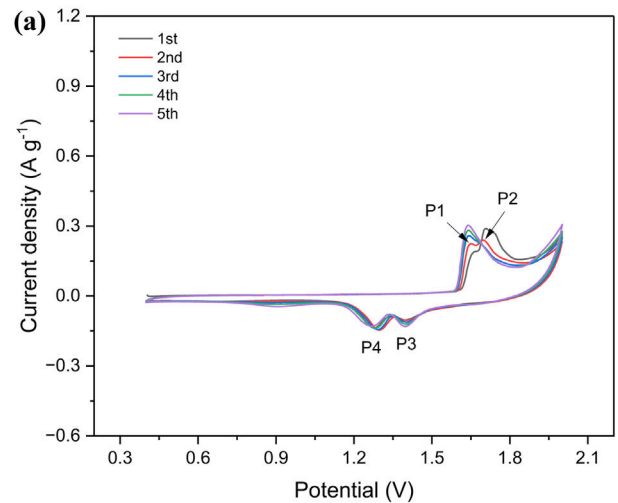
The CV tests were performed to evaluate the electrochemical performance of the synthesized ZMO cathode materials. Fig. 10 displays the CV curves of ZIBs utilizing ZMO-0Co and ZMO-0.45Co at a scan rate of 0.5 mV/s within the voltage range of 0.2–2.2V. Two pairs of distinct redox peaks are

Table 2 – Equivalent circuit parameters of EIS of the ZIBs using ZMO-0Co and ZMO-0.45Co with a voltage of 10 mV and frequency range of 0.1 Hz to 100 kHz.

Sample	R_s (Ω)	R_{ct} (Ω)	Q ($\Omega^{-1} S^n$)	n	σ ($\Omega s^{0.5}$)
ZMO-0Co	2.8	72	6.8×10^{-4}	0.78	11.2
ZMO-0.45Co	3.5	48	1.1×10^{-3}	0.82	9.5

**Fig. 8 – N₂ adsorption–desorption isotherms of ZnMn₂O₄ at different Co concentrations: ZMO-0Co, ZMO-0.15Co, ZMO-0.3Co, and ZMO-0.45Co.****Fig. 9 – Nyquist plots and equivalent circuit of ZIBs using ZMO-0Co and ZMO-0.45Co with a voltage of 10 mV and frequency range of 0.1 Hz to 100 kHz.**

evident in both cathodic and anodic sweeps, indicating the occurrence of multistep reaction processes [71]. The anodic peaks observed at approximately 1.60 V and 1.70 V correspond to the extraction of Zn²⁺ ions from the peanut-shaped ZMO, in conjunction with the oxidation of Mn³⁺ to Mn⁴⁺ during the charging process. In contrast, the cathodic peaks located at around 1.40 V and 1.20 V are associated with the insertion

**Fig. 10 – CV curves of ZIBs using (a) ZMO-0Co, and (b) ZMO-0.45Co with a scan rate of 0.5 mV/s and voltage range of 0.2–2.2 V for the first to fifth cycles.**

of Zn²⁺ ions into ZMO and the reduction of Mn⁴⁺ to a lower valence state during discharge, suggesting the restoration of MnO₂ in peanut-shaped ZnMn₂O₄ structure [72,73]. The small separation between the anodic and cathodic peak potentials (ΔE_p) implies that the Zn²⁺ intercalation/deintercalation process is highly reversible and kinetically favorable. In particular, the narrower ΔE_p observed for ZMO-0.45Co compared with ZMO-0Co indicates that Co substitution facilitates faster charge-transfer kinetics and improved electrochemical reversibility. Furthermore, the nearly overlapping CV curves from the first to fifth cycles demonstrate the excellent electrochemical stability and reproducibility of the electrode

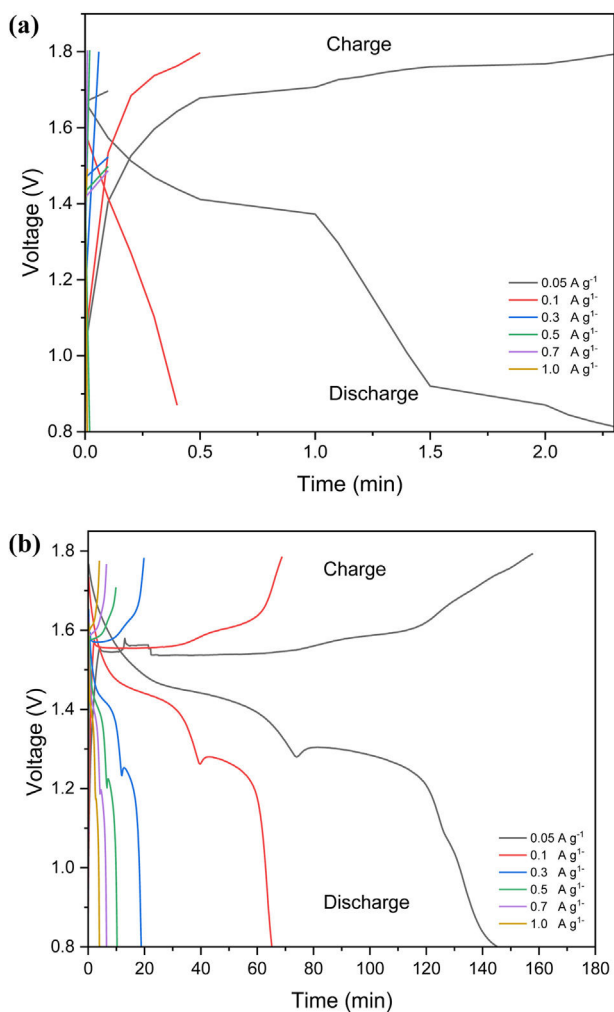


Fig. 11 – Voltage profiles of ZIBs using (a) ZMO-0Co, and (b) ZMO-0.45Co at current densities of 0.05, 0.1, 0.3, 0.5, 0.7, and 1.0 $A g^{-1}$.

materials. As the scan rate increases, the redox peaks shift slightly toward higher potentials during the anodic scans and lower potentials during cathodic scans, indicating diffusion-controlled behavior [74,75]. Co-doping enhances both the reversibility of Zn^{2+} insertion/extraction and the pseudo-capacitive behavior of ZMO, resulting in faster kinetics and higher specific capacity. Therefore, the ZMO-0.45Co cathode exhibits a larger CV peak area and higher redox peak intensity compared with ZMO-0Co, reflecting its enhanced specific capacity and more efficient charge transfer performance.

Fig. 11 illustrates the GCD curve of ZIBs at current densities of 0.05, 0.1, 0.3, 0.5, 0.7, and 1.0 $A g^{-1}$ employing ZMO-0Co and ZMO-0.45Co cathode materials. This curve displays two distinct sloping voltage platforms on the charge–discharge curves, corresponding to the two pairs of reduction/oxidation peaks [76] in the CV curve (Fig. 10). The two platforms found in the discharge curve are indicative of the intercalation processes involving H^+ and Zn^{2+} ions. The ZMO-0.45Co electrode demonstrates a more stable and prolonged discharge platform in comparison to the pristine ZMO electrode, suggesting that the incorporation of Co doping and oxygen defects signifi-

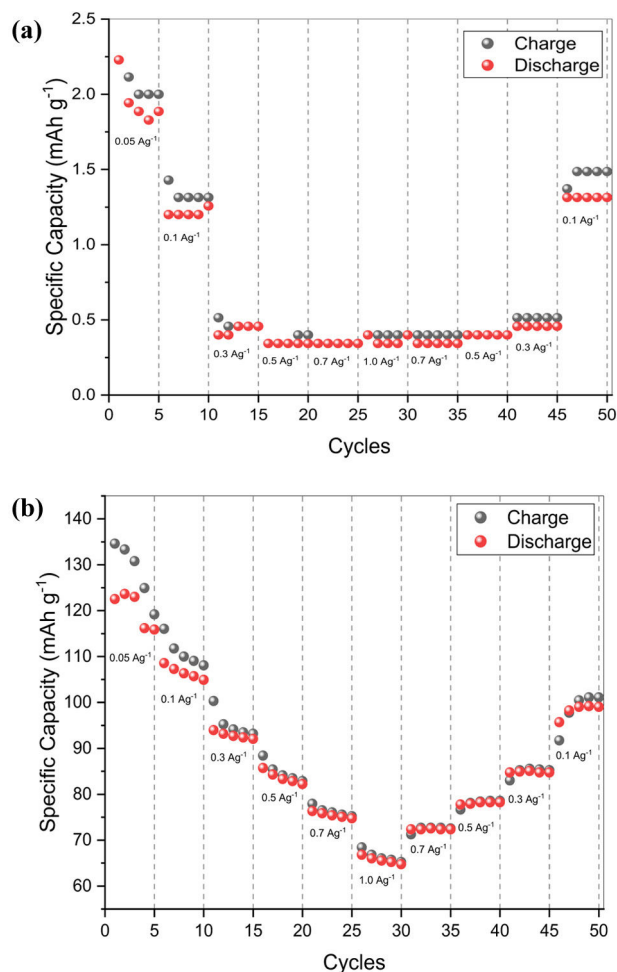


Fig. 12 – Rate capability of ZIBs using (a) ZMO-0Co, and (b) ZMO-0.45Co at series current densities of 0.05, 0.1, 0.3, 0.5, 0.7, and 1.0 $A g^{-1}$ with 5 cycles in each current.

cantly improves the capacity of this electrode [70]. Moreover, enhancing the specific capacity in the initial cycles validates the activation process [77].

To further demonstrate the outstanding characteristics of the peanut-shaped Co-doped ZMO, an investigation of the rate capability and long-term cycling stability is conducted, with a comparison to the pristine ZMO. Fig. 12 presents a comparative analysis of the specific capacities of ZIBs utilizing ZMO-0Co and ZMO-0.45Co cathode at various current densities of 0.05, 0.1, 0.3, 0.5, 0.7, and 1.0 $A g^{-1}$, with data collected over 5 cycles for each current density. Both materials clearly show reduced capacities as the current rate increases. In the case of pure ZMO cathode, the presence of a hollow and porous nanostructure is overshadowed by its inherent low electronic conductivity. Additionally, the pulverization and cracking of $ZnMn_2O_4$ nanoparticles lead to a rapid decline in capacity [78,79]. For the $Zn_{1-x}Co_xMn_2O_4$ ($x=0.45$) electrode, with increasing current density and extended cycle times, the maximum charge and discharge values reach 133.0 and 122.5 $mAh g^{-1}$, respectively. It consistently demonstrates significantly enhanced rate performance compared to pure $ZnMn_2O_4$.

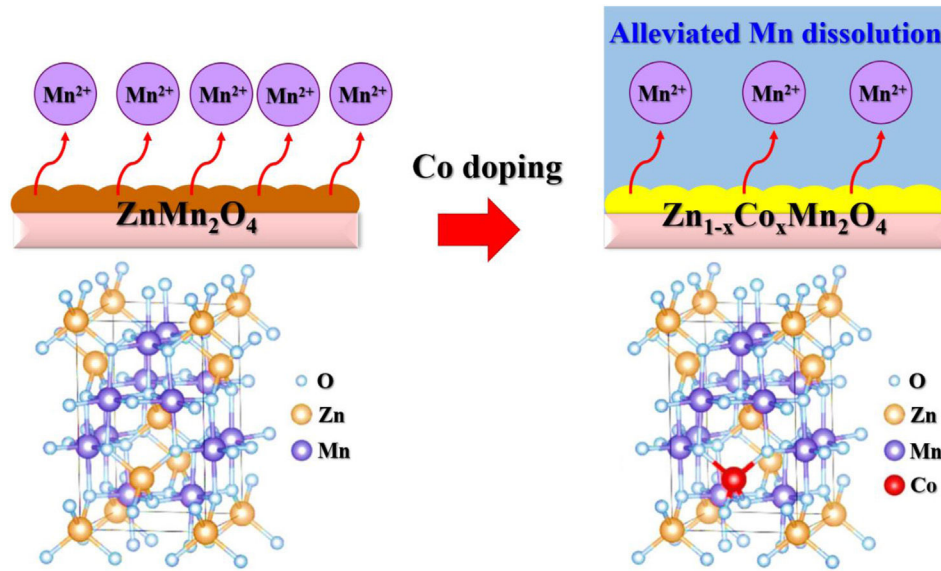


Fig. 13 – Co doping reduces active material loss and improves capacity of ZMO via alleviated Mn dissolution.

Table 3 – A comparative study of cathode materials for ZIBs, including synthesis method, electrolyte, potential window, specific capacity, and cycle performance.

Cathode material	Synthesis method	Electrolyte	Potential window (V)	Specific capacity (mAh g ⁻¹)	Cycle performance (mAh g ⁻¹)	Reference
ZMO-0.45Co	Solvothermal/calcination	2 M ZnSO ₄	0.4–1.8	133 (at 0.05 A g ⁻¹)	101 (after 50 cycles at 0.1 A g ⁻¹)	Our work
Ag ₂ V ₄ O ₁₁	Hydrothermal	3 M Zn(CF ₃ SO ₃) ₂	0.3–1.3	252 (at 0.5 A g ⁻¹)	118 (after 1000 cycles at 3.0 A g ⁻¹)	[80]
CaV ₆ O ₁₆ ·3H ₂ O	Hydrothermal	3 M Zn(CF ₃ SO ₃) ₂	0–1.4	320 (at 0.05 A g ⁻¹)	125 (after 70 cycles at 4.0 A g ⁻¹)	[81]
Cu ₃ V ₂ O ₇ (OH) ₂ ·2H ₂ O	Hydrothermal	2.5 M Zn(CF ₃ SO ₃) ₂	0.2–1.6	216 (at 0.1 A g ⁻¹)	92 (after 500 cycles at 0.5 A g ⁻¹)	[82]

Based on this study, the problem of stability degradation in ZnMn₂O₄ owing to Mn³⁺ dissolution could be resolved by Co doping (Fig. 13). In general, as the number of cycles increases, the specific capacity of ZnMn₂O₄ decreases due to structural and electrochemical changes during cycling. One probable reason involves the MnO_x deposition on ZnMn₂O₄ samples [32]. The introduction of Co²⁺ in ZnMn₂O₄ changes a fraction of Mn³⁺ into Mn⁴⁺ in order to maintain charge balance. This results in a decrease in Mn³⁺ content, suppression of Mn dissolution, and improved cycling stability. Overall, Co-doped ZnMn₂O₄ demonstrates significantly improved long-term cycling stability when compared to pristine ZnMn₂O₄, making it as a promising electrode material. However, structural stability during charge-discharge cycles is still limited for long-term usage.

Table 3 compares the performance of several reported cathode materials for ZIBs [80–82] in terms of synthesis method, electrolyte, potential window, specific capacity, and cycling

stability. The Co-doped ZnMn₂O₄ (ZMO-0.45Co) prepared in this work exhibits a moderate potential window (0.4–1.8 V) and delivers a specific capacity of 133 mAh g⁻¹ at 0.05 A g⁻¹, with 101 mAh g⁻¹ retained after 50 cycles. Although vanadium (V)-based cathodes show higher initial capacities, they typically involve more complex synthesis routes and higher material costs. In contrast, ZMO-0.45Co demonstrates a well-balanced combination of good cycling stability, enhanced conductivity, and environmental friendliness, making it a promising and cost-effective cathode material for aqueous ZIBs.

Conclusion

Here, we present peanut-shaped Co-doped ZnMn₂O₄ (ZMO) as a cathode material for ZIBs, synthesized via a simple solvothermal reaction followed by a post-calcination

process. The resulting porous $Zn_{1-x}Co_xMn_2O_4$ ($x = 0.45$) material exhibited a high specific capacity of 133.0 mAh g^{-1} at 0.05 A g^{-1} , along with reasonable cycling stability, and rate capability. Co doping in ZMO enhanced charge transfer performance and specific capacity, while reducing Mn dissolution in the cathode material of ZIBs. Owing to its improved electrochemical performance, the novel ZMO-0.45Co sample shows great potential as a cathode material for next-generation ZIBs. Furthermore, this simple strategy can be applied to design other ZMO-based materials with porous architectures that possess promising energy storage and conversion properties due to their unique structural features.

Conflict of interest

The authors confirm that there are no known financial conflicts or personal connections that might seem to have impacted the research presented in this paper.

Acknowledgements

The authors would also like to thank the Department of Materials Science and Engineering, Faculty of Engineering and Industrial Technology, Silpakorn University for their assistance and support. The authors would additionally like to acknowledge the Department of Materials Science, Faculty of Science, Chulalongkorn University for providing materials, chemicals, and battery testing instruments.

REFERENCES

- [1] W. Habib, A. Saji, F. Paul, P.R. Markapudi, C. Wilson, L. Manjakkal, Flexible electrochemical capacitors based on ZnO-carbon black composite, *Results Eng.* 25 (2025), 104510, <http://dx.doi.org/10.1016/j.rineng.2025.104510>.
- [2] A. Buasri, T. Chinaphong, P. Muangkum, A. Telakul, V. Loryuenyong, Green synthesis of reduced graphene oxide using pomelo peel and its application in electrochromic device, *AIP Conf. Proc.* 2397 (2021), 070006, <http://dx.doi.org/10.1063/5.0063824>.
- [3] M.A. Alemu, A.K. Worku, M.Z. Getie, Recent advancement of electrically rechargeable alkaline metal-air batteries for future mobility, *Results Chem.* 6 (2023), 101048, <http://dx.doi.org/10.1016/j.rechem.2023.101048>.
- [4] L. Tang, H. Peng, J. Kang, H. Chen, M. Zhang, Y. Liu, D.H. Kim, Y. Liu, Z. Lin, Zn-based batteries for sustainable energy storage: strategies and mechanisms, *Chem. Soc. Rev.* 53 (2024) 4877–4925, <http://dx.doi.org/10.1039/D3CS00295K>.
- [5] G.A. Begaw, D.W. Ayele, A.K. Worku, T.A. Wubieneh, T.A. Yemata, M.D. Ambaw, Recent advances and challenges of cobalt-based materials as air cathodes in rechargeable Zn-air batteries, *Results Chem.* 5 (2023), 100896, <http://dx.doi.org/10.1016/j.rechem.2023.100896>.
- [6] A. Buasri, T. Ananganjanakit, N. Peangkom, P. Khantasema, K. Pleeram, A. Lakaao, J. Arthnukarn, V. Loryuenyong, A facile route for the synthesis of reduced graphene oxide (RGO) by DVD laser scribing and its applications in the environment-friendly electrochromic devices (ECD), *J. Optoelectron. Adv. Mater.* 19 (2017) 492–500.
- [7] X. Liang, R. Xiao, X. Liao, Preparation of lithium iron phosphate composites by electrodeposition with a tunnel structure on aluminium foil surface, *Bol. Soc. Esp. Ceram. Vidr.* 59 (2020) 251–258, <http://dx.doi.org/10.1016/j.bscev.2019.12.003>.
- [8] V. Loryuenyong, J. Khamsawat, P. Danwong, A. Buasri, P. Pattananuwat, Application of coffee silverskin cellulose/polyacrylamide gel polymer electrolytes for rechargeable zinc-ion batteries, *Sci* 6 (2024) 50, <http://dx.doi.org/10.3390/sci6030050>.
- [9] V. Loryuenyong, B. Plongmai, N. Pajantorn, P. Pattananuwat, A. Buasri, Sustainable zinc-ion battery separators based on silica and cellulose fibers derived from coffee parchment waste, *J. Compos. Sci.* 9 (2025) 452, <http://dx.doi.org/10.3390/jcs9080452>.
- [10] M. Sharma, R. Sharma, Zn-ion batteries: $ZnMn_2O_4$ as cathode material, *Mater. Today Proc.* 26 (2020) 3378–3385, <http://dx.doi.org/10.1016/j.matpr.2019.10.152>.
- [11] J. Liu, C. Xu, Z. Chen, S. Ni, Z.X. Shen, Progress in aqueous rechargeable batteries, *Green Energy Environ.* 3 (2018) 20–41, <http://dx.doi.org/10.1016/j.gee.2017.10.001>.
- [12] Q. Chen, Q. Wang, Q. Ma, Q.Q. Song, Q. Chen, Influence of surface coating on structure and properties of metallic lithium anode for rechargeable Li- O_2 battery, *Bol. Soc. Esp. Ceram. Vidr.* 56 (2017) 64–72, <http://dx.doi.org/10.1016/j.bscev.2016.10.002>.
- [13] X. Meng, Z. Cheng, L. Li, The promotion of research progress of zinc manganate cathode materials for zinc-ion batteries by characterization and analysis technology, *Molecules* 28 (2023), 4459, <http://dx.doi.org/10.3390/molecules28114459>.
- [14] J. Cao, D. Zhang, X. Zhang, Z. Zeng, J. Qin, Y. Huang, Strategies of regulating Zn^{2+} solvation structures for dendrite-free and side reaction-suppressed zinc-ion batteries, *Energy Environ. Sci.* 15 (2022) 499–528, <http://dx.doi.org/10.1039/D1EE03377H>.
- [15] L. Li, S. Jia, Z. Cheng, C. Zhang, Improved strategies for separators in zinc ion batteries, *ChemSusChem* 16 (2023), e202202330, <http://dx.doi.org/10.1002/cssc.202202330>.
- [16] L. Li, S. Jia, M. Cao, Y. Ji, H. Qiu, D. Zhang, Research progress on transition metal sulfide-based materials as cathode materials for zinc-ion batteries, *J. Energy Storage* 67 (2023), 107614, <http://dx.doi.org/10.1016/j.est.2023.107614>.
- [17] GopiF C.V.V.M., R. Ramesh, Review of battery-supercapacitor hybrid energy storage systems for electric vehicles, *Results Eng.* 24 (2024), 103598, <http://dx.doi.org/10.1016/j.rineng.2024.103598>.
- [18] S. Yang, L. Zhang, M. Luo, Y. Cui, J. Wang, D. Zhao, C. Yang, X. Wang, B. Cao, Synergistic combination of a Co-doped σ - MnO_2 cathode with an electrolyte additive for a high-performance aqueous zinc-ion battery, *ChemPhysMater* 2 (2023) 77–82, <http://dx.doi.org/10.1016/j.chphma.2022.04.007>.
- [19] S. Yang, M. Zhang, X. Wu, X. Wu, F. Zeng, Y. Li, S. Duan, D. Fan, Y. Yang, X. Wu, The excellent electrochemical performances of $ZnMn_2O_4/Mn_2O_3$: the composite cathode material for potential aqueous zinc ion batteries, *J. Electroanal. Chem.* 832 (2019) 69–74, <http://dx.doi.org/10.1016/j.jelechem.2018.10.051>.
- [20] W. Panloetparnich, V. Loryuenyong, A. Buasri, Facile synthesis of polyaniline-nickel oxide composites via interfacial polymerization, *Mater. Today Proc.* 52 (2021) 2485–2489, <http://dx.doi.org/10.1016/j.matpr.2021.10.435>.
- [21] N. Wang, J. Yin, H. Li, T. Wang, S. Cui, W. Yan, W. Liu, Y. Jin, Recent advance in Mn-based Li-rich cathode materials: oxygen release mechanism and its solution strategies based on electronic structure perspective, spanning from commercial liquid batteries to all-solid-state batteries, *Next Mater.* 6 (2025), 100408, <http://dx.doi.org/10.1016/j.nxmate.2024.100408>.
- [22] Y. Zhang, P. Zhang, Y. Xu, X. Song, H. Wang, T. Ma, Synthesis of pomegranate-shaped micron $ZnMn_2O_4$ with enhanced lithium storage capability, *J. Mater.* 7 (2021) 699–707, <http://dx.doi.org/10.1016/j.jmat.2021.01.005>.
- [23] Z. Zheng, Y. Cheng, X. Yan, R. Wang, P. Zhang, Enhanced electrochemical properties of graphene-wrapped $ZnMn_2O_4$ nanorods for lithium-ion batteries, *J. Mater. Chem.* 2 (2014) 149–154, <http://dx.doi.org/10.1039/c3ta13511j>.

- [24] G. Zhang, L. Yu, H.B. Wu, H.E. Hoster, X.W. Lou, Formation of ZnMn_2O_4 ball-in-ball hollow microspheres as a high-performance anode for lithium-ion batteries, *Adv. Mater.* 24 (2012) 4609–4613, <http://dx.doi.org/10.1002/adma.201201779>.
- [25] J. Zou, B. Liu, H. Liu, Y. Ding, T. Xin, Y. Wang, Facile synthesis of interconnected mesoporous ZnMn_2O_4 nano-peanuts for Li-storage via distinct structure design, *Mater. Res. Bull.* 107 (2018) 468–476, <http://dx.doi.org/10.1016/j.materresbull.2018.08.019>.
- [26] F. Wang, H. Dai, S. Chen, J. Li, Y. Wang, Synthesis of peanut-shaped porous ZnMn_2O_4 microparticles with enhanced lithium storage properties, *J. Mater. Sci. Mater. Electron.* 31 (2020) 20632–20640, <http://dx.doi.org/10.1007/s10854-020-04583-1>.
- [27] I.D. Anyaogu, A.C. Nwanya, F.I. Ezema, P.M. Ejikeme, Cobalt ion-doped polyvinyl alcohol: a promising multivalent polymer electrolyte system for aluminium – air battery application, *Hybrid Adv.* 8 (2025), 100369, <http://dx.doi.org/10.1016/j.hybadv.2024.100369>.
- [28] S.A. Getaneh, A.G. Temam, G.A. Workneh, A.C. Nwanya, P.M. Ejikeme, F.I. Ezema, Advances in MoS_2 -based ternary nanocomposites for high-performance electrochemical energy storage, *Hybrid Adv.* 7 (2024), 100333, <http://dx.doi.org/10.1016/j.hybadv.2024.100333>.
- [29] L. Ma, Z. Wei, X. Zhu, J. Liang, X. Zhang, Synthesis and photocatalytic properties of Co-doped $\text{Zn}_{1-x}\text{Co}_x\text{Mn}_2\text{O}$ hollow nanospheres, *J. Nanomater.* 2019 (2019), 4257270, <http://dx.doi.org/10.1155/2019/4257270>.
- [30] X. Zhu, Z. Wei, L. Ma, J. Liang, X. Zhang, Synthesis and electrochemical properties of Co-doped ZnMn_2O_4 hollow nanospheres, *Bull. Mater. Sci.* 43 (2020) 4, <http://dx.doi.org/10.1007/s12034-019-1970-6>.
- [31] Sk.K. Hussain, J.S. Yu, Cobalt-doped zinc manganese oxide porous nanocubes with controlled morphology as positive electrode for hybrid supercapacitors, *Chem. Eng. J.* 361 (2019) 1030–1042, <http://dx.doi.org/10.1016/j.cej.2018.12.152>.
- [32] S.C. Kang, C.-W. Hyeon, S.-Y. Yoo, J.Y. Park, Y.J. Kim, C.-Y. Chung, S.-E. Chun, A stable ZnMn_2O_4 cathode for aqueous Zn-ion batteries via Ni doping to suppress Mn dissolution, *J. Alloys Compd.* 1010 (2025), 177165, <http://dx.doi.org/10.1016/j.jallcom.2024.177165>.
- [33] S. Sun, Y. Lin, Q. Yan, X. Zhu, Regulating the crystal structure of ZnMn_2O_4 material by Zr doping for rechargeable aqueous zinc-ion batteries, *Electrochim. Acta* 520 (2025), 145900, <http://dx.doi.org/10.1016/j.electacta.2025.145900>.
- [34] S. Vinoth, M. Govindasamy, S.-F. Wang, A.A. Allothman, R.A. Alshgari, Hydrothermally synthesized cubical zinc manganite nanostructure for electrocatalytic detection of sulfadiazine, *Microchim. Acta* 188 (2021) 131, <http://dx.doi.org/10.1007/s00604-021-04768-3>.
- [35] S. Aouini, A. Bardaoui, A.M. Ferrara, D.M.F. Santos, R. Chtourou, ZnMn_2O_4 nanopyrramids fabrication by hydrothermal route: Effect of reaction time on the structural, morphological, and electrochemical properties, *Energies* (2022) 9352, <http://dx.doi.org/10.3390/en15249352>.
- [36] C. Shamitha, T. Senthil, L. Wu, B.S. Kumar, S. Anandhan, Sol-gel electrosputted mesoporous ZnMn_2O_4 nanofibers with superior specific surface area, *J. Mater. Sci. Mater. Electron.* 28 (2017) 15846–15860, <http://dx.doi.org/10.1007/s10854-017-7479-0>.
- [37] N. Yadav, S. Khamhsanga, S. Kheawhom, J. Qin, P. Pattanauwat, MnCo_2O_4 spinel microsphere assembled with flake structure as a cathode for high-performance zinc ion battery, *J. Energy Storage* 64 (2023), 107148, <http://dx.doi.org/10.1016/j.est.2023.107148>.
- [38] T. Huang, C. Zhao, Z. Qiu, J. Luo, Z. Hu, Hierarchical porous ZnMn_2O_4 synthesized by the sucrose-assisted combustion method for high-rate supercapacitors, *Ionics* 23 (2017) 139–146, <http://dx.doi.org/10.1007/s11581-016-1817-8>.
- [39] P. Zhang, X. Li, Q. Zhao, S. Liu, Synthesis and optical property of one-dimensional spinel ZnMn_2O_4 nanorods, *Nanoscale Res. Lett.* 6 (2011) 323, <http://dx.doi.org/10.1186/1556-276X-6-323>.
- [40] L.S. Lobo, A.R. Kumar, Investigation of structural and electrical properties of ZnMn_2O_4 synthesized by sol-gel method, *J. Mater. Sci. Mater. Electron.* 27 (2016) 7398–7406, <http://dx.doi.org/10.1007/s10854-016-4714-z>.
- [41] C. Yuan, L. Zhang, S. Zhu, H. Cao, J. Lin, L. Hou, Heterostructured core-shell ZnMn_2O_4 nanosheets@carbon nanotubes' coaxial nanocables: a competitive anode towards high-performance Li-ion batteries, *Nanotechnology* 26 (2015), 145401, <http://dx.doi.org/10.1088/0957-4484/26/14/145401>.
- [42] S. Guillemet-Fritsch, C. Chanel, J. Sarrias, S. Bayonne, A. Rousset, X. Alcobe, M.L.M. Sarrion, Structure, thermal stability and electrical properties of zinc manganites, *Solid State Ion.* 128 (2000) 233–242, [http://dx.doi.org/10.1016/S0167-2738\(99\)00340-9](http://dx.doi.org/10.1016/S0167-2738(99)00340-9).
- [43] P.E. Saranya, S. Selladurai, Efficient electrochemical performance of ZnMn_2O_4 nanoparticles with rGO nanosheets for electrodes in supercapacitor applications, *J. Mater. Sci. Mater. Electron.* 29 (2018) 3326–3339, <http://dx.doi.org/10.1007/s10854-017-8268-5>.
- [44] N. Acharya, R. Sagar, Comparative study on structure, dielectric and electrical properties of cobalt- and zinc-substituted Mn_3O_4 spinels, *Appl. Phys. A: Mater. Sci. Process.* 126 (2020) 515, <http://dx.doi.org/10.1007/s00339-020-03659-3>.
- [45] Y. Zong, Y. Sun, S. Meng, Y. Wang, H. Xing, X. Li, X. Zheng, Doping effect and oxygen defects boost room temperature ferromagnetism of Co-doped ZnO nanoparticles: experimental and theoretical studies, *RSC Adv.* 9 (2019) 23012–23020, <http://dx.doi.org/10.1039/C9RA03620B>.
- [46] M.A.M. Khan, M.W. Khan, M. Alhoshan, M.S. AlSalhi, A.S. Aldwayyan, Influences of Co doping on the structural and optical properties of ZnO nanostructured, *Appl. Phys. A: Mater. Sci. Process.* 100 (2010) 45–51, <http://dx.doi.org/10.1007/s00339-010-5840-8>.
- [47] P. Patra, I. Naik, H. Bhatt, S.D. Kaushik, Structural, infrared spectroscopy and magnetic properties of spinel ZnMn_2O_4 , *Phys. B: Condens. Matter.* 572 (2019), 199–202, <http://dx.doi.org/10.1016/j.physb.2019.08.005>.
- [48] P. Ahuja, R.K. Sharma, G. Singh, Solid-state, high-performance supercapacitor using graphene nanoribbons embedded with zinc manganite, *J. Mater. Chem. A* 3 (2015) 4931–4937, <http://dx.doi.org/10.1039/c4ta05865h>.
- [49] Z.K. Heiba, M.B. Mohamed, A. Badaw, Structural and optical properties of $(1-x)\text{ZnMn}_2\text{O}_4/x\text{PbS}$ nanocomposites, *J. Mater. Sci. Mater. Electron.* 33 (2022) 11354–11364, <http://dx.doi.org/10.1007/s10854-022-08108-w>.
- [50] Z.K. Heiba, M.B. Mohamed, S.I. Ahmed, Modifying the structure and optical characteristics of ZnMn_2O_4 by alloying with CdS to form heterostructure nanocomposite, *Appl. Phys. A: Mater. Sci. Process.* 127 (2021) 883, <http://dx.doi.org/10.1007/s00339-021-05021-7>.
- [51] R.A. Nasr, A.F. El-Sayed, G.M.E. Komy, G.T. El-Bassyouni, S.M. Mousa, Modification of photocatalytic activity and antibacterial properties of Mn_2O_3 by Zn ions doping, *Sci. Rep.* 15 (2025), 14325, <http://dx.doi.org/10.1038/s41598-025-95769-2>.
- [52] C.R. Mariappan, R. Kumar, G.V. Prakash, Functional properties of ZnCo_2O_4 nano-particles obtained by thermal decomposition of a solution of binary metal nitrates, *RSC Adv.* 5 (2015), 26843, <http://dx.doi.org/10.1039/c5ra01937k>.
- [53] K. Samanta, P. Bhattacharya, R.S. Katiyar, Optical properties of $\text{Zn}_{1-x}\text{Co}_x\text{O}$ thin films grown on Al_2O_3 (0001) substrates, *Appl. Phys. Lett.* 87 (2005), 101903, <http://dx.doi.org/10.1063/1.2039995>.
- [54] M. Dekkers, G. Rijnders, D.H.A. Blank, ZnIr_2O_4 , a p-type transparent oxide semiconductor in the class of spinel

- zinc-d⁶-transition metal oxide, *Appl. Phys. Lett.* 90 (2007), 021903, <http://dx.doi.org/10.1063/1.2431548>.
- [55] Y. Lu, Y. Lin, D. Wang, L. Wang, T. Xie, T. Jiang, A high performance cobalt-doped ZnO visible light photocatalyst and its photogenerated charge transfer properties, *Nano Res.* 4 (2011) 1144–1152, <http://dx.doi.org/10.1007/s12274-011-0163-4>.
- [56] L. Luo, H. Qiao, K. Chen, Y. Fei, Q. Wei, Fabrication of electrospun ZnMn₂O₄ nanofibers as anode material for lithium-ion batteries, *Electrochim. Acta* 177 (2015) 283–289, <http://dx.doi.org/10.1016/j.electacta.2015.01.100>.
- [57] S. Zhu, Q. Chen, C. Yang, Y. Zhang, L. Hou, G. Pang, X. He, X. Zhang, C. Yuan, Biomorphic template-engaged strategy towards porous zinc manganate micro-belts as a competitive anode for rechargeable lithium-ion batteries, *Int. J. Hydrogen Energy* 42 (2017) 14154–14165, <http://dx.doi.org/10.1016/j.ijhydene.2017.04.197>.
- [58] M.F. Khan, A.H. Ansari, M. Hameedullah, M.B. Lohani, M.M. Alam, Z.A. AlOthman, A.M. Khan, M.K. Khan, Synthesis, characterization, modeling and anti-bacterial properties of peanut-shaped ZnO nano-bunches, *Nano Hybrids* (2013) 61–85, <http://dx.doi.org/10.4028/www.scientific.net/NH.4.61>.
- [59] T. Dippong, F. Goga, E.-A. Levei, O. Cadar, Influence of zinc substitution with cobalt on thermal behaviour, structure and morphology of zinc ferrite embedded in silica matrix, *J. Solid State Chem.* 275 (2019) 159–166, <http://dx.doi.org/10.1016/j.jssc.2019.04.011>.
- [60] F. Barkat, M. Afzal, B.S. Khan, A. Saeed, M. Bashir, A. Mukhtar, T. Mehmood, K. Wu, Formation mechanism and lattice parameter investigation for copper-substituted cobalt ferrites from *Zingiber officinale* and *Elettaria cardamom* seed extracts using biogenic route, *Materials* 15 (2022), 4374, <http://dx.doi.org/10.3390/ma15134374>.
- [61] M.N. Nawaz, U. Ghazanfar, W. Yuan, H. Wahab, O.T. Satti, S.B. Khan, Impact of cobalt doping on the properties of zinc ferrite (Co_xZn_{1-x}Fe₂O₄), *J. Mater. Sci. Mater. Electron.* 36 (2025) 790, <http://dx.doi.org/10.1007/s10854-025-14770-7>.
- [62] H. Palani, A. Rastogi, Effect of annealing temperature on structural and electrochemical behaviour on MgFe₂O₄ as electrode material in neutral aqueous electrolyte for supercapacitors, *Nanotechnology* 35 (2024), 175401, <http://dx.doi.org/10.1088/1361-6528/ad1e96>.
- [63] D. Papadaki, G.H. Mhlongo, D.E. Motaung, S.S. Nkosi, K. Panagiotaki, E. Christaki, M.N. Assimakopoulos, V.C. Papadimitriou, F. Rosei, G. Kiriakidis, S.S. Ray, Hierarchically porous Cu-, Co-, and Mn-doped platelet-like ZnO nanostructures and their photocatalytic performance for indoor air quality control, *ACS Omega* 4 (2019) 16429–16440, <http://dx.doi.org/10.1021/acsomega.9b02016>.
- [64] Y.L. Wang, X.Q. Wei, N. Guo, X.L. Deng, X.J. Xu, Synthesis and characterization of Cd-doped ZnMn₂O₄ microspheres as supercapacitor electrodes, *J. Mater. Sci. Mater. Electron.* 28 (2017) 1223–1228, <http://dx.doi.org/10.1007/s10854-016-5649-0>.
- [65] M.S. Choubari, S. Rahmani, J. Mazloom, Boosted electrochemical performance of magnetic caterpillar-like Mg_{0.5}Ni_{0.5}Fe₂O₄ nanospinel as a novel pseudocapacitive electrode material, *Sci. Rep.* 13 (2023), 7822, <http://dx.doi.org/10.1038/s41598-023-35014-w>.
- [66] Z.R. Khan, M. Shkir, V. Ganesh, I.S. Yahia, S. AlFaify, A facile microwave-assisted synthesis of novel ZnMn₂O₄ nanoparticles and their structural, morphological, optical, surface area, and dielectric studies, *Indian J. Phys.* 95 (2021) 43–49, <http://dx.doi.org/10.1007/s12648-020-01695-6>.
- [67] V. Doiphode, P. Vairale, V. Sharma, A. Waghmare, A. Punde, P. Shinde, S. Shah, S. Pandharkar, Y. Hase, R. Aher, S. Nair, V. Jadkar, B. Bade, M. Prasad, S. Rondiya, S. Jadkar, Solution-processed electrochemical synthesis of ZnFe₂O₄ photoanode for photoelectrochemical water splitting, *J. Solid State Electrochem.* 25 (2021) 1835–1846, <http://dx.doi.org/10.1007/s10008-021-04953-7>.
- [68] J. Leva-Bueno, S.A. Peyman, P.A. Millner, A review on impedimetric immunosensors for pathogen and biomarker detection, *Med. Microbiol. Immunol.* 209 (2020) 343–362, <http://dx.doi.org/10.1007/s00430-020-00668-0>.
- [69] X. Liu, R. Deng, X. Wei, Z. Chen, Q. Zheng, C. Xu, D. Lin, Mg²⁺ and Mn²⁺ bimetallic co-doped Na₃V₂(PO₄)₃ as advanced cathode for sodium-ion batteries, *J. Alloys Compd.* 895 (2022), 162511, <http://dx.doi.org/10.1016/j.jallcom.2021.162511>.
- [70] Y. Yang, T. Shao, Y. Zhang, Y. Lu, M. Li, H. Liu, Q. Xu, Y. Xia, Anionic S-doping of a ZnMn₂O₄/CNTs cathode material enhances its Zn²⁺ storage performance in aqueous zinc-ion batteries, *J. Power Sources* 564 (2023), 232863, <http://dx.doi.org/10.1016/j.jpowsour.2023.232863>.
- [71] D. Feng, T.-N. Gao, L. Zhang, B. Guo, S. Song, Z. Qiao, S. Dai, Boosting high-rate zinc-storage performance by the rational design of Mn₂O₃ nanoporous architecture cathode, *Nano-Micro Lett.* 12 (2020) 14, <http://dx.doi.org/10.1007/s40820-019-0351-4>.
- [72] L. Qin, Q. Zhu, L. Li, H. Cheng, W. Li, Z. Fang, M. Mo, S. Chen, Ni²⁺-doped ZnMn₂O₄ with enhanced electrochemical performance as cathode material for aqueous zinc-ion batteries, *J. Solid State Electrochem.* 27 (2023) 773–784, <http://dx.doi.org/10.1007/s10008-022-05370-0>.
- [73] S. Xu, H. Xiong, Z. Wang, H. Ma, X. Sun, P. Wang, J. Zhu, X.-R. Shi, Electrochemical activated ZnMn₂O₄ with Al doping for boosting high-capacity and long-term stable Zn ion storage, *J. Energy Storage* 122 (2025), 116711, <http://dx.doi.org/10.1016/j.est.2025.116711>.
- [74] Z. Masood, H. Muhammad, I.A. Tahir, Comparison of different electrochemical methodologies for electrode reactions: a case study of paracetamol, *Electrochem* 5 (2024) 57–59, <http://dx.doi.org/10.3390/electrochem5010004>.
- [75] O. Taran, Electron transfer between electrically conductive minerals and quinones, *Front. Chem.* 5 (2017) 49, <http://dx.doi.org/10.3389/fchem.2017.00049>.
- [76] T. Shao, Y. Zhang, T. Cao, Y. Yang, Z. Li, H. Liu, Y. Wang, Y. Xia, Structural regulation of ZnMn₂O₄ cathode material by K, Fe-double doping to improve its rate and cycling stability for rechargeable aqueous zinc-based batteries, *Chem. Eng. J.* 431 (2022), 133735, <http://dx.doi.org/10.1016/j.cej.2021.133735>.
- [77] S. Saadi-motaalleg, M. Javanbakht, H. Omidvar, S. Habibzadeh, A novel Ni-doped ZnMn₂O₄/Mn₂O₃ nanocomposite synthesized by pulsed potential as superior zinc ion battery cathode material, *J. Alloys Compd.* 963 (2023), 171119, <http://dx.doi.org/10.1016/j.jallcom.2023.171119>.
- [78] W. Zhou, D. Wang, L. Zhao, C. Ding, X. Jia, Y. Du, G. Wen, H. Wang, Template-free fabrication of graphene-wrapped mesoporous ZnMn₂O₄ nanorings as anode materials for lithium-ion batteries, *Nanotechnology* 28 (2017), 245401, <http://dx.doi.org/10.1088/1361-6528/aa6ec4>.
- [79] L. Zhou, H.B. Wu, T. Zhu, X.W.(D.) Lou, Facile preparation of ZnMn₂O₄ hollow microspheres as high-capacity anodes for lithium-ion batteries, *J. Mater. Chem.* 22 (2012) 827–829, <http://dx.doi.org/10.1039/c1jm15054e>.
- [80] X. Tong, J. Zhong, X. Hu, F. Zhang, Preparation and performance of highly stable cathode material Ag₂V₄O₁₁ for aqueous zinc-ion battery, *Crystals* 13 (2023) 565, <http://dx.doi.org/10.3390/cryst13040565>.
- [81] N. Xu, X. Lian, H. Huang, Y. Ma, L. Li, S. Peng, CaV₆O₁₆·3H₂O nanorods as cathode for high-performance aqueous zinc-ion battery, *Mater. Lett.* 287 (2021), 129285, <http://dx.doi.org/10.1016/j.matlet.2020.129285>.
- [82] L. Chen, Z. Yang, J. Wu, H. Chen, J. Meng, Energy storage performance and mechanism of the novel copper pyrovanadate Cu₃V₂O₇(OH)₂·2H₂O cathode for aqueous zinc ion batteries, *Electrochim. Acta* 330 (2020), 135347, <http://dx.doi.org/10.1016/j.electacta.2019.135347>.